

The effect of vibrational relaxation on the discharge coefficient of critical flow venturis¹

A.N. Johnson^{a,*}, J.D. Wright^a, S. Nakao^b, C.L. Merkle^c, M.R. Moldover^a

^a National Institute of Standards and Technology (NIST), Gaithersburg, MD, USA

^b National Research Laboratory of Metrology (NRLM), Tsukuba, Japan

^c H.H. Arnold Chair, University of Tennessee Space Institute, Tullahoma, USA

Received 10 September 1999; received in revised form 8 December 1999; accepted 8 December 1999

Abstract

This paper identifies a new mechanism that can affect the discharge coefficient of critical nozzle flows. Specifically, vibrational relaxation effects are demonstrated to significantly influence the discharge coefficient of selected gases in critical venturi flows. This phenomenon explains why certain gases — like carbon dioxide — exhibit calibration characteristics that differ significantly from other gases (e.g., N₂, O₂, Ar, He, and H₂). A mathematical model is developed which predicts this behavior, and vibrational non-equilibrium effects are further substantiated by two independent experiments. © 2000 Elsevier Science Ltd. All rights reserved.

1. Introduction

Critical nozzles (also known as critical flow venturis) provide a reliable and precise way of measuring gas mass flow and play an important role in many industrial processes. These devices have numerous industrial applications including uses as gas flow meters, mass flow controllers, calibration standards for other gas flow meters, and pressure isolators. Moreover, because critical nozzles are robust, offer a high degree of repeatability, and maintain their calibration performance for long periods of time [1], these devices are often used as a transfer standards for international comparisons among national metrology institutes (NMI's), and for disseminating flow traceability from NMI's to secondary laboratories domestically [2,3].

In an effort to reduce flowrate measurement uncertainty and extend the range of flows and gas compositions allowed by critical nozzle applications, there has been an increased interest on improving the understanding of the flow behavior in these devices. One aspect in particular involves understanding how gas composition affects the mass flow through critical nozzles. From a

practical standpoint it would be advantageous to calibrate a critical nozzle for one gas composition, but apply the nozzle using a different gas specie. In this paper a mathematical model is proposed — based on first principles — that characterizes the effect of gas species in critical nozzle flows.

The geometry of sonic nozzles has been standardized by the International Organization for Standardization (ISO) [4] to promote uniformity within the flow metering community. In this geometry (see Fig. 1), the entrance converging section profile is mathematically described by a circular arc of constant curvature which contracts down to a minimum cross sectional area at a location known as the *nozzle throat*. In the ISO standard, the circular arc extends past the nozzle throat to a point of tangency where the wall shape becomes conical. The conical shape is maintained at a constant angle for the remainder of the divergent section.

For a critical nozzle to operate according to ISO specifications, the ratio of back pressure downstream of the nozzle exit plane to the upstream pipeline stagnation pressure (P_b/P_0) must be maintained below a critical threshold known as the *critical pressure ratio*. Under this condition, the subsonic gas flow in the upstream piping is accelerated to sonic velocities (i.e. $M=1$) at the nozzle throat. Given that flow disturbances propagate through the fluid as pressure waves traveling at the speed of sound, these disturbances cannot propagate upstream

* Corresponding author. Tel: +1-301-258-9201.

E-mail address: anj100@jet.nist.gov (A.N. Johnson).

¹ This paper is declared a work of the US Government and is not subject to copyright protection in the United States.

Nomenclature

A^*	venturi throat area
C_s	critical flow factor= $\sqrt{\gamma \left(\frac{\gamma+1}{2}\right)^{\frac{(\gamma+1)}{2(1-\gamma)}}$
C_d	discharge coefficient
c_v	specific heat at constant volume
d	venturi throat diameter
D	approach pipe diameter
L	characteristic length along a streamline
\dot{m}	mass flow rate
M	mach number
M_w	molecular weight
P	pressure
R	venturi throat radius= $d/2$
R_c	radius of curvature at nozzle throat
R_e	Reynolds number based on diameter= $4\dot{m}/(\pi\mu_0d)$
R_{gas}	gas constant= R_u/M_w
R_u	universal gas constant
r	radius or radial coordinate
s	arc length along a streamline
T	temperature
x	axial coordinate
u	axial component of velocity
v	radial component of velocity
z	dimensionless length along a streamline= s/L

Greek

δ^*	displacement thickness, satisfies $(R-\delta^*)^2 = \int_0^R (2r\rho u)/(\overline{\rho u})_{\text{inv}} dr$
γ	specific heat ratio
Γ	time ratio= $\tau_{\text{vib}}/\tau_{\text{res}}$
ε	thermodynamic internal energy
ε_0	zero point energy
ε_{rot}	molecular rotational energy
$\varepsilon_{\text{trans}}$	molecular translational energy
ε_{vib}	molecular vibrational energy
θ	half angle of nozzle divergent section= 0.05236 radians (3°)
μ	molecular viscosity
ρ	density
T_{res}	residence time
T_{vib}	vibrational relaxation time

Subscripts

ideal	based on one-dimensional inviscid analysis
inv	based on a multi-dimensional inviscid analysis
o	stagnation condition
real	based on experimental data

Superscripts

*	throat conditions based on one-dimensional inviscid theory
eq	based on equilibrium flow
fr	based on frozen flow

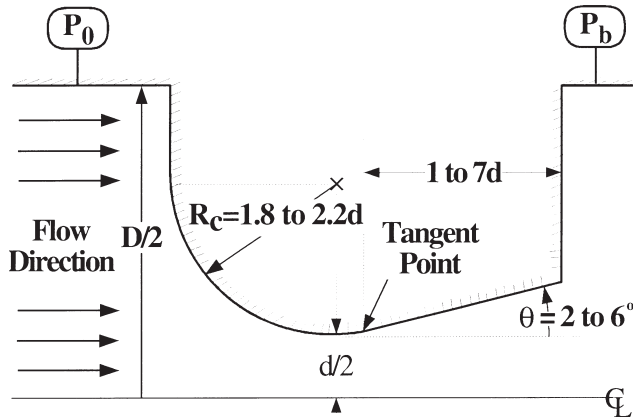


Fig. 1. Schematic of a critical nozzle: D =approach pipe diameter, d =nozzle throat diameter, θ =nozzle divergent half angle.

against oncoming supersonic flow. As a result, once sonic conditions are obtained at the nozzle throat, the region upstream of the throat is effectively isolated from down-stream disturbances. This condition is commonly referred to as *choked* flow or *choking* of the nozzle. Ideally, under choked flow conditions the mass flow through the device depends only on upstream stagnation conditions and is entirely independent of any changes in flow conditions downstream of the throat.

In the ISO standard, the divergent section of the critical nozzle plays a key role functioning as a pressure recovery element that extends the flow range capabilities of the device by increasing the minimum critical pressure ratio necessary to choke the nozzle. Without the presence of the divergent section, the operation of the critical nozzle would be more costly given that the pressure drop across the resulting device would be significantly larger than the one obtained by the ISO geometry.

Under *idealized* conditions (i.e. inviscid one-dimensional flow of a calorically perfect ideal gas) a closed form expression for the mass flow in a critical nozzle has been found in the following form [5]

$$\dot{m}_{ideal} = \frac{P_0 A^* C_s}{\sqrt{R_{gas} T_0}} \quad (1)$$

In this expression, the subscript *ideal* emphasizes the simplifications used in this formulation of the mass flow. Generally speaking Eq. (1) will overpredict the actual mass flow through a critical nozzle by roughly 1–10% (depending on Reynolds number), mostly attributed to the presence of a boundary layer in the real flow. Multi-dimensional effects, which result in curvature of the sonic line, also reduce the actual mass flow below \dot{m}_{ideal} , but generally to a lesser extent since the throat radius of curvature for ISO nozzles has been carefully selected to minimize this effect [6,7].

For applications requiring greater accuracy, the idealized expression for mass flow given in Eq. (1) is sup-

plemented by defining the dimensionless discharge coefficient

$$C_d \equiv \frac{\dot{m}_{real}}{\dot{m}_{ideal}} \quad (2)$$

where the actual mass flow, \dot{m}_{real} can be either estimated using more complex analytical models [8–11] or measured experimentally [12,13]. Experimental calibration offers advantages over analytical methods given that the experimental errors can be estimated to yield an overall expanded uncertainty for the procedure [14]. For this reason experimental calibrations are generally considered more accurate than analytical approaches where fewer methods exist for estimating errors caused by any assumptions required. Nevertheless, analytical models can prove useful given that they often serve as a guide to experimental calibration providing physical insight into the processes that cause deviations from ideal conditions.

For a given nozzle geometry, the discharge coefficient changes as a function of the flow rate through it. Traditionally, this functionality has been expressed in terms of a reference Reynolds number defined as [15]

$$Re_{ideal}^* = \frac{4\dot{m}_{ideal}}{\pi d \mu_0} \quad (3)$$

where d is the nozzle throat diameter and μ_0 is the molecular viscosity evaluated at stagnation conditions. Here the Reynolds number has been defined based on the ideal mass flow, \dot{m}_{ideal} , but in experimental work the Reynolds number is often based on the actual mass flow, \dot{m}_{real} . The discharge coefficient relates both versions of Reynolds number, $C_d = Re_{real}^* / Re_{ideal}^*$.

Fig. 2 compares experimental calibration data of Nakao et al. [16] with the analytical predictions of Ishibashi and Takamoto [11] for several gases. The experimental measurements were taken at Reynolds numbers in the

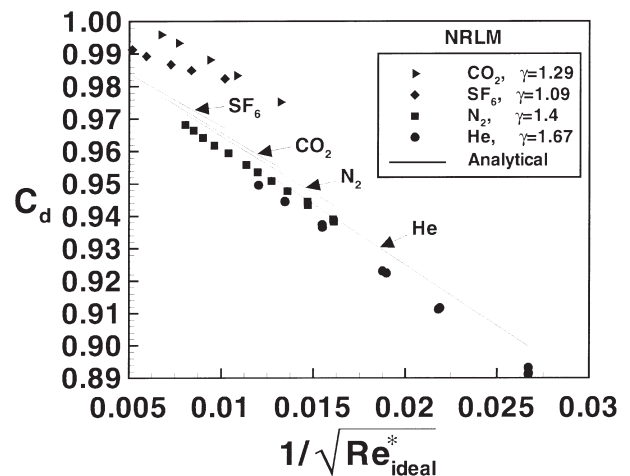


Fig. 2. Experimental and analytic calibration curves for various gas species flowing through a critical nozzle: $d=0.5935$ mm, $\theta=3^\circ$.

laminar flow range using a small throat diameter ($d=0.5935$ mm) ISO critical nozzle. Following the results of previous analytical investigations [9,10] and experimental observations [4,11], the experimental data has been linearized by plotting C_d vs $1/\sqrt{Re_{ideal}^*}$. This method of linearization works because C_d (to first order) is directly proportional to the displacement thickness, δ^* , which varies inversely with the square root of Reynolds number for laminar flows. The experimental data also depicts how viscous effects influence the discharge coefficient. At high Reynolds numbers (i.e. low $1/\sqrt{Re_{ideal}^*}$) boundary layer thins and C_d increases for all the gases considered. The size of the symbols used in this figure is indicative of the 0.2% experimental uncertainty. The variation of calibration data among the different gas species indicates that C_d is not fully characterized by Reynolds number alone, but has a functional dependence on gas species as well. Moreover, a more complete characterization of C_d must include additional parameters that account for physical phenomena excluded by the traditional Reynolds number characterization.

The analytic predictive model used in Fig. 2 was developed in 1997 by Ishibashi and Takamoto [11] by synthesizing the results of two previously published models [8,9]. They combined the axisymmetric compressible boundary layer model of Gerrop [9] with an axisymmetric inviscid compressible flow model for the core flow developed by Hall [8]. The model of Ishibashi and Takamoto therefore accounts for both viscous and multi-dimensional effects that are present in the real flow. This analytic model characterizes C_d in terms of both Re_{ideal}^* and γ , thereby correcting the calibration data by accounting for varying γ among gas species. Nakao et al. demonstrated that this correction works quite well for several gases (e.g. He, Ar, H₂, N₂, and O₂), predicting C_d behavior to within a few tenths of a percent [16]. However, for other gases (e.g. CO₂ and SF₆) the Ishibashi and Takamoto model underpredicts C_d by more than 2% — an error level unacceptable for high accuracy metering applications.

In 1998, Johnson et al. [17] investigated the C_d characteristics of CO₂ in small throat diameter critical nozzles using Computational Fluid Dynamics (CFD). This approach solves the full compressible Navier–Stokes equations, avoiding many of the simplifying assumptions used in the previous analytical models. The CFD model, however, yielded no noticeable improvement over the analytical models. The fact that neither the composite boundary layer/inviscid core model of Ishibashi and Takamoto nor the more general CFD model accurately predicted the C_d behavior for CO₂, suggested that important physical phenomena may be absent in both of these models.

Ishibashi and Takamoto [11] hypothesized that condensation of CO₂ might be responsible for the discrepancy between analytical C_d predictions and the experi-

mental data. This was unlikely, however, since the local temperatures throughout the nozzle remained above the saturation temperature. Johnson et al. [17] in previous work also considered and ruled out several possible explanations for the unique CO₂ behavior: C_d dependence on Prandtl number, heat transfer at the nozzle wall, and nozzle installation effects associated with predictive models. In the present paper, non-equilibrium thermodynamic processes caused by vibrational relaxation are demonstrated to be the likely explanation for the observed species effect for CO₂. (The explanation for the unique SF₆ calibration behavior are still being investigated.)

2. Numerical method

2.1. Governing equations

In small-scale critical nozzles the flow is accelerated from nearly stagnant upstream conditions to sonic conditions at the nozzle throat over small distances (i.e., about 1 mm for the calibration data in Fig. 2). Consequently, flow residence times are short (about 10^{-6} s), leaving insufficient time for the vibrational energy of the flowing gas molecules to equilibrate with the changing thermodynamic environment.² This phenomenon, known as *vibrational non-equilibrium* and sometimes referred to as *vibrational relaxation*, can play an appreciable role in critical nozzle flow processes when the following conditions are met:

1. Spatial temperature gradients exist within the flow field.
2. The vibrational relaxation time (i.e. the time necessary for a thermodynamic system to redistribute its vibrational energy when subjected to a new thermodynamic environment) is greater than or equal to the flow residence time ($\tau_{vib} \geq \tau_{res}$).
3. The vibrational energy makes a non-negligible contribution to the overall internal energy of the gas.

The laws of thermodynamics require that gases in the freestream expand as they accelerate through a critical nozzle. This isentropic expansion process causes the temperature of the expanding gas to decrease along the nozzle length, thereby ensuring condition (1) is met for critical nozzle flows. The remaining two conditions, however, are only realized by certain gas species. Simpler molecules (i.e. the diatomic molecules: H₂, O₂, and N₂) relax slowly, but do not have sufficient vibrational

² Translational and rotational modes relax much faster than vibrational modes and therefore equilibrate with the local thermodynamic environment

energy at normal operating temperatures (around 300 K) for vibrational relaxation effects to be important [i.e. condition (3) is not satisfied]. On the other hand, larger, more complex molecules frequently do have sufficient vibrational energy even at room temperature. Nevertheless, most equilibrate quickly so that condition (2) is not satisfied.

An order of magnitude analysis can be used to determine which gases are likely to experience vibrational relaxation effects. A brief analysis is presented here that quantifies conditions (2) and (3) for selected gases, first for N_2 and then CO_2 . To make this analysis definitive we consider the small throat diameter ($d=0.5395$ mm) ISO nozzle that was calibrated in Fig. 2, and we determine the internal energy, the vibrational energy, and the vibrational relaxation time at a suitable reference temperature and pressure of 300 K and 101,325 Pa respectively. For N_2 , the average flow residence time can be estimated by dividing the appropriate length scale (i.e. the distance from the nozzle inlet to the nozzle throat) by the average velocity over this distance. When the average velocity is estimated by using one-dimensional ideal flow theory, the average flow residence time is on the order of 10^{-6} s. The vibrational relaxation time for N_2 (at the reference condition) is on the order of 10^{-5} s. Since N_2 equilibrates nearly an order of magnitude slower than the average residence time, vibrational relaxation effects could be important if N_2 's vibrational energy levels are sufficiently populated. At the reference temperature of 300 K, only 0.0056% of N_2 's overall internal energy is stored as vibrational energy. Consequently, although condition (2) indicates that N_2 flow is not in vibrational equilibrium, the negligible level of vibrational energy allows these non-equilibrium effects to be neglected. For CO_2 the vibrational relaxation time is on the same order of magnitude as the average flow residence time so that vibrational relaxation effects are present in the flow field. Unlike N_2 , however, the contribution of vibrational energy of CO_2 represents 5.6% of the overall internal energy. As a result, vibrational non-equilibrium phenomena could play a role in the gas dynamics of CO_2 flow.

When vibrational non-equilibrium effects are important, they are primarily an issue in the inviscid core region of critical nozzle flows where they alter thermodynamic and flow processes. At the nozzle inlet the gas (taken to be thermally perfect herein) is locally in equilibrium, and the internal energy is a function of temperature alone, $\varepsilon=\varepsilon(T)$. As the fluid element is accelerated through the converging section of the nozzle, however, the vibrational energy, ε_{vib} , never adjusts to the ever decreasing downstream temperatures, causing the flow to deviate further and further from equilibrium behavior with advancing downstream distances. Consequently, non-equilibrium behavior must be considered, and the

internal energy becomes a function of two variables, $\varepsilon=\varepsilon(T, \varepsilon_{vib})$.

To model critical nozzle flows with vibrational non-equilibrium effects included, a deterministic method is required to predict the local value of vibrational energy, ε_{vib} , throughout the flow field. Molecular theory provides such an expression — the vibrational rate equation [18]. For the purposes of this paper a form of the the vibrational rate equation valid for steady flows along a streamlines³ is implemented as given below

$$\Gamma \frac{d\varepsilon_{vib}}{dz} = \varepsilon_{vib}^{eq} - \varepsilon_{vib}. \quad (4)$$

In this expression ε_{vib} is the local non-equilibrium value of vibrational energy, ε_{vib}^{eq} is the local equilibrium value of vibrational energy, $z=s/L$ is the dimensionless arc length along a Streamline, and $\Gamma=\tau_{vib}/\tau_{res}$, is the ratio of local vibrational relaxation time to the residence time. The local residence time, $\tau_{res}=L/||\mathbf{u}||$, is defined in terms of $||\mathbf{u}||$, the local magnitude of fluid velocity, and L , the characteristic length along a streamline. The vibrational relaxation time decreases with increasing pressure or temperature according to the relation of Landau and Teller [19]. A commonly used low temperature approximation of their relationship is given as [18]

$$\tau_{vib} = K_1 \frac{\exp(K_2/T)^{1/3}}{P} \quad (5)$$

where the constants K_1 and K_2 depend on properties of the molecule. For CO_2 the constants, $K_1=4.205 \times 10^{-2}$ Pa/s and $K_2=10,635.1$ K, were determined by fitting Eq. (5) to experimental data [20] over a temperature range from 200 to 300 K. The equilibrium vibrational energy is a function of temperature following the relationship

$$\varepsilon_{vib}^{eq}(T) = \int_{T_{ref}}^T c_v(T) dT + \varepsilon(T_{ref}) - \varepsilon_{trans}(T) - \varepsilon_{rot}(T) - \varepsilon_0 \quad (6)$$

where the constant volume specific heat, $c_v(T)=a_0+a_1T$, is a linear curve fit to CO_2 data for a perfect gas [21], $\varepsilon_{trans}=3/2R_{gas}T$ is the molecular translational energy, and $\varepsilon_{rot}=R_{gas}T$ is the molecular rotational energy for the linear triatomic CO_2 molecule, and ε_0 is the zero-point energy. Note that the contribution of electronic energy is negligible over the temperature range of interest and is not included in the above expression. The reference temperature, T_{ref} , and the reference internal energy, $\varepsilon(T_{ref})$,

³ By following streamlines the vibrational rate equation, which is generally a partial differential equation, is reduced to an ordinary differential equation.

are arbitrary and both are taken to be zero.⁴ Analogously, the zero-point energy, ϵ_0 , is also taken as zero.

To model vibrational non-equilibrium flow in critical nozzles the vibrational rate equation [i.e. Eq. (4)] must be solved simultaneously with the equations governing fluid motion — the steady, axisymmetric, compressible Navier–Stokes equations. In this work, CO₂ gas is considered thermally perfect (i.e. $P=\rho R_{\text{gas}}T$), and non-equilibrium effects are included in the definition of internal energy given as

$$\epsilon = \frac{5}{2}R_{\text{gas}}T + \epsilon_{\text{vib}} \quad (7)$$

where the term, $\frac{5}{2}R_{\text{gas}}T$, represents the sum of translational and rotational energy. The effects of turbulence are not considered herein given that the Reynolds numbers range (2500–131,000) is much lower than the experimentally observed transition Reynolds number for critical nozzles (10^6) [22].

2.2. Numerical algorithm

The solution of the non-equilibrium flow field is obtained by globally iterating between the Navier–Stokes equations and the vibrational rate equation [i.e. Eq. (4)] in such a manner as to ensure that both are simultaneously satisfied. Below we first briefly discuss the procedure used to solve the Navier–Stokes equations and then describe the method used to integrate the vibrational rate equation. An overview of the coupling between the two solutions is then given.

2.2.1. Solution of Navier–Stokes equation

The numerical solution of the compressible form of the Navier–Stokes equations is obtained by means of an implicit time marching procedure. In this approach, the time derivatives are retained in the equations of motion and used to march the solution to steady state. To provide improved convergence over a range of Mach numbers and Reynolds numbers, the physical time derivatives are modified by both inviscid and viscous preconditioning [23–25].

As a first step in the numerical solution, the Navier–Stokes equations are transformed to a generalized body-fitted coordinate system. These generalized equations are then discretized in both space and time. The convective terms are discretized by means of a third-order flux difference-split up-wind scheme, while the diffusive terms are treated by central differences. The time derivatives are replaced by first-order backward differences. The resulting implicit system is then solved by alternating

direction implicit factorization. The resulting block tridiagonal matrices are inverted using a block version of the Thomas algorithm at each time step. The equation system is closed by using the perfect gas equation of state to relate the fluid density to the pressure and temperature. Thermodynamic properties (molecular viscosity and thermal conductivity) are obtained from curve fits to experimental data [21].

2.2.2. Solution of vibrational rate equation

In contrast to the Navier–Stokes equations which are expressed in an Eulerian sense, the vibrational rate equation is expressed in a Lagrangian sense. Specifically, this equation describes the rate of relaxation of the vibrational modes of a gas particle of fixed identity as it moves through the flowfield. The Lagrangian paths of particles of fixed identity correspond to streamlines in the flowfield. The trajectories of these streamlines must be estimated from the Navier–Stokes solution before the vibrational rate equation can be solved. In the coupling procedure between the two equation sets, the streamlines in the flowfield are computed after each time step using the most recent approximation to the Navier–Stokes solution. The vibrational rate equation [Eq. (4)] is then solved on each streamline by a space-marching procedure that integrates between consecutive points on a streamline (see Fig. 3).

Integrating the vibrational rate equation along streamlines provides a convenient method for including relaxation effects, however, this procedure presents a minor difficulty. In general, grid points do not coincide with streamlines and interpolation is necessary to find the streamlines. To improve accuracy and provide a more straightforward integration procedure without interpolation, the grid system was adjusted after each iteration to lie on the streamlines computed from the most recent time-step of the Navier–Stokes equations. The

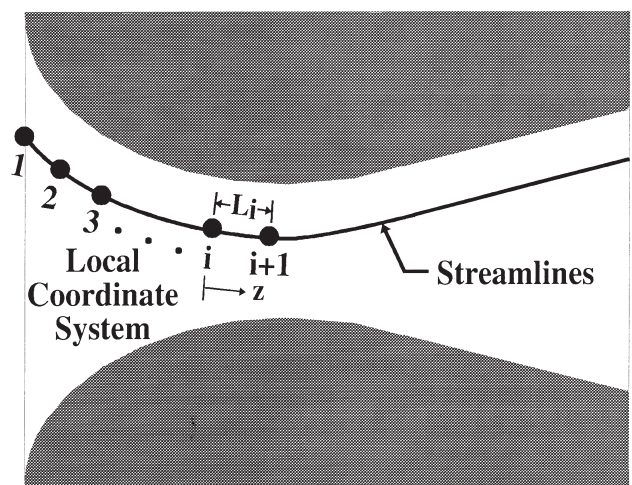


Fig. 3. Schematic illustrating local coordinate frame used for solving the vibrational rate equation.

⁴ The constant energy datum is determined by T_{ref} and $\epsilon(T_{\text{ref}})$, but this reference value plays no role in thermodynamic processes.

vibrational rate equation was then integrated on this new grid system to obtain the relaxation rates at each point in the flow field. The Navier–Stokes equations were also solved on the new grid at the next time step. As convergence is approached, the grid system becomes stationary, and the Navier–Stokes and the vibrational rate equation are solved on the same, streamline-oriented grid system. Consequently, the need for interpolation is eliminated.

In computing the solution for the vibrational rate equation, the coefficient $\Gamma = \tau_{\text{vib}}/\tau_{\text{res}}$ and the source term $\varepsilon_{\text{vib}}^{\text{eq}}$ are both evaluated from the latest solution of the Navier–Stokes equation. The space-marching procedure starts at the nozzle inlet where the vibrational energy on each streamline (each grid line) is equal to its equilibrium value (i.e. $\varepsilon_{\text{vib}}^1 = \varepsilon_{\text{vib}}^{\text{eq}}(T_1)$). The integration procedure (herein done analytically by variation of parameters [26]) determines ε_{vib} at the next grid point. In turn, this value of ε_{vib} serves as an initial condition for the next point, and so on, until the complete streamline has been updated. This process is then repeated for each streamline in the flowfield. The calculated value of vibrational energy, ε_{vib} , is used to determine the thermodynamic internal energy in [Eq. (7)], which in turn, is used to update the Navier–Stokes equations. Consequently the Navier–Stokes solution depends upon the vibrational rate solution and conversely. We also mention that this non-equilibrium model, just described, reduces to the equilibrium model for gas species not satisfying the previously mentioned conditions (1)–(3).

2.3. Computational domain and boundary conditions

The computational domain included only the converging–diverging nozzle region of Fig. 1 shown earlier and neglected the piping sections. The omission of the piping sections is strictly a matter of convenience to enable attention to be directed to the effects of vibrational relaxation. Previous solutions show that including the inlet pipe section reduces C_d by approx. 0.1%. As a result, we tolerate this small offset in C_d in the present computations. The grid for this geometry consisted of 201 grid points in the axial direction and 101 grid points in the radial direction.

The grid cells in the radial direction were concentrated near the wall in order to resolve the large gradients present in the boundary layer region. Computations on both coarser and finer grids indicated that this level of discretization gave grid-independent results for the present problem.

Boundary conditions are specified at the nozzle inlet and outlet, along the nozzle wall, and along the axis of symmetry. At the nozzle inlet T_0 , P_0 , and the flow angle are specified. (Note including the inlet pipe section would improve this somewhat.) Because the flow is assumed to exit at supersonic velocities, extrapolation of all characteristic variables is applied at the exit plane

in accordance with the method of characteristics [27]. Symmetry conditions are applied along the centerline, and an adiabatic, no-slip boundary condition is applied along the impermeable nozzle wall.

3. Results

Experimental data taken for several gas species (shown previously in Fig. 2 shows that traditional calibration curves (i.e. C_d vs Re_{ideal}^* plots) are species dependent. In the following results the proposed vibrational non-equilibrium model for CO_2 is validated by direct comparison with the experimental data of Nakao et al. [16]. In addition the results from the previous analytical [11] and equilibrium CFD [17] models are included to help quantify the level of improvement rendered by including non-equilibrium effects. The numerical simulations follow the experimental calibration procedure by holding the stagnation temperature fixed ($T_0=300$ K) while varying the stagnation pressure ($25,331.25 \text{ Pa} \leq P_0 \leq 202,650 \text{ Pa}$) to yield Re_{ideal}^* in the range from 5700 to 22 000.

The calibration curves shown in Fig. 4 compare C_d predictions of three mathematical models to experimental data. The experimental data is labeled by the \bullet 's where the size of the symbol is indicative of the 0.2% experimental uncertainty. Each of the mathematical models offers a different level of complexity. The simplest of these models is the composite boundary layer/inviscid core model of Ishibashi and, Takamoto represented by the dashed line (---). In this model the specific heat ratio is assumed constant ($\gamma=1.29$) to permit a closed form algebraic expression for the discharge coefficient. A closely related but slightly more refined

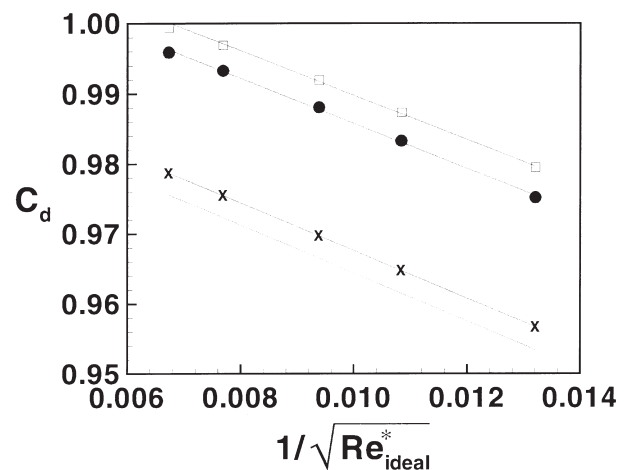


Fig. 4. Comparison between mathematical models and experimental data for CO_2 flow through an ISO critical nozzle ($d=0.5395$ mm and $\theta=3^\circ$): NRLM analytical model with $\gamma=1.29$ (---), equilibrium CFD model with a temperature dependent γ (\times), non-equilibrium CFD model (\square), and experimental data (\bullet).

analysis (—×—) uses the equilibrium CFD model to predict C_d behavior. In the equilibrium CFD model the full Navier Stokes equations are solved, and a more physical temperature dependent specific heat ratio is utilized [i.e. $\gamma=\gamma(T)$]. The present model (—□—) incorporates vibrational non-equilibrium effects into the CFD algorithm.

The C_d predictions of all three models are found to have good qualitative agreement with the experimental data over the entire range of Re_{ideal}^* . In particular, the four curves are linear with nearly equal slopes. Each model differs from experimental C_d values by a nearly uniform offset, where the magnitude and sign of the offset varies for each model. The analytical model of Ishibashi and Takamoto ($\gamma=constant$) yields the largest offset, underpredicting the experimental C_d by more than 2%. The equilibrium CFD model [$\gamma=\gamma(T)$] provides a modest improvement, underpredicting the experimental results by slightly less than 2%. The vibrational relaxation model provides the best agreement with the experimental data, overpredicting experimental C_d 's by only 0.4%.

The slight C_d overprediction for CO_2 is consistent with overpredictions observed when the analytical model [11] (or equilibrium flow model [17]) is used to predict C_d behavior for Ar, H_2 , and N_2 — gases not affected by vibrational relaxation. Therefore, it is plausible that the slight C_d overprediction is caused by physical mechanisms absent in all three models. For example, not including the upstream piping has been shown to result in an overprediction of C_d by approx. 0.1%. Also, the adiabatic wall boundary condition used in the computations has been estimated in previous work [17] to cause a slight overprediction in C_d ranging from 0.05 to 0.1% depending on the Reynolds number.

Non-equilibrium flow processes are responsible for the more than 2% increase in C_d between the equilibrium flow model (—×—) and the non-equilibrium flow model (—□—) in Fig. 4. Physically, vibrational relaxation effects induce increased mass flows, which in turn, lead to increased C_d 's. The reason for the increase in mass flow is two fold: first, flow acceleration processes are augmented, resulting in higher freestream throat velocities. Second, the flow expansion through the critical nozzle is diminished leading to higher freestream throat densities. The combined effect is illustrated in Fig. 5, which compares the non-equilibrium radial mass flux profile (i.e. ρu) to the corresponding equilibrium profile at the throat for $Re_{ideal}^*=2402$. In the figure, ρu has been conveniently normalized by ρ^*u^* (i.e. the predicted mass flux for ideal flow conditions) so that an area weighted integration across the throat cross section yields the discharge coefficient. The nearly 2% increase in the freestream mass flux observed for non-equilibrium flow in Fig. 5, is therefore responsible for the 2% offset between equilibrium and non-equilibrium C_d predictions in Fig. 4.

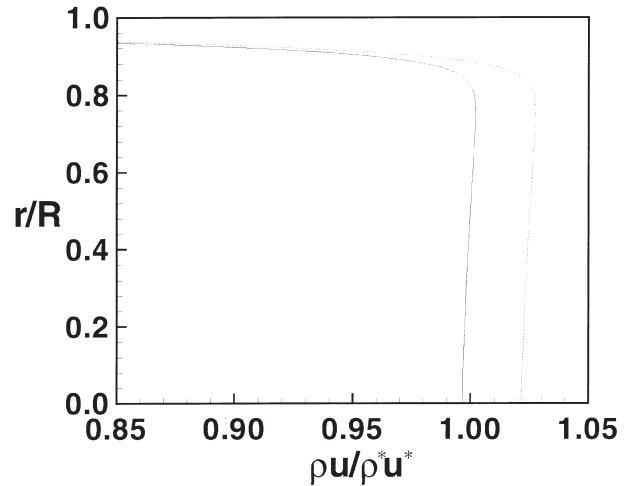


Fig. 5. Comparison of normalized throat mass flux profile for equilibrium CFD model [$\gamma=\gamma(T)$], and non-equilibrium CFD model at $Re_{ideal}^*=2402$: equilibrium CFD model (—), non-equilibrium CFD model (---).

3.1. Limiting cases of non-equilibrium flow

Due to the complexity of non-equilibrium flow processes, a rigorous consideration of this phenomenon requires computer modeling. However, a qualitative understanding of C_d behavior can be obtained by considering the two limiting cases of vibrational non-equilibrium flow — *equilibrium flow and frozen flow*. Mathematically, both of these limiting cases are controlled by $\Gamma=\tau_{vib}/\tau_{res}$, the ratio of relaxation time to residence time [refer to Eq. (4)]. Equilibrium flow occurs in the limit as Γ tends toward zero (i.e. $\Gamma\rightarrow 0$). In the equilibrium flow limit the CO_2 molecules comprising the fluid element immediately adjust their vibrational energy level to the decreasing surrounding temperature. Mathematically, the left hand side of Eq. (4) vanishes (i.e. a singular perturbation problem) so that the vibrational energy obtains its equilibrium value.⁵ From this it follows that the internal energy, $\epsilon^{eq}(T)$, the specific heat at constant volume, $c_v^{eq}(T)=d\epsilon/dT$, and the specific heat ratio, $\gamma^{eq}(T)=1+R_{gas}/c_v^{eq}$ are all functions of temperature only, where the superscript, “eq”, emphasizes equilibrium flow.

Frozen flow, on the other hand, occurs in the limit as the ratio of relaxation time to residence time tends toward infinity (i.e. $\Gamma\rightarrow\infty$). In the frozen flow limit the CO_2 molecules comprising the fluid element have no time to adjust their vibrational energy level to the decreasing freestream temperatures. Consequently, the vibrational energy remains *frozen* at its upstream equilibrium value. Mathematically, as Γ tends toward infinity the right-hand side of Eq. (4) vanishes (i.e. a regular

⁵ At the nozzle inlet the ϵ_{vib} is in equilibrium so that a perturbation analysis not necessary

perturbation problem) so that the spatial derivative of ε_{vib} on the left-hand side is identically zero, and ε_{vib} remains constant (i.e. $\varepsilon_{\text{vib}}=\text{constant}$) throughout the flow field. Moreover, since the flow is in equilibrium at the nozzle inlet, the constant value of vibrational energy is equal to the inlet equilibrium value. It follows that for frozen flow the internal energy, $\varepsilon^{\text{fr}}(T)=\frac{5}{2}R_{\text{gas}}T+\text{constant}$, is a linear function of temperature [see Eq. (7)]. Accordingly, the frozen flow constant volume specific heat, $c_{\text{V}}^{\text{fr}}=\frac{5}{2}R_{\text{gas}}$, and the frozen flow specific heat ratio, $\gamma^{\text{fr}}=1.4$, are both constant.

By comparing equilibrium flow to frozen flow, general conclusions can be drawn about how vibrational non-equilibrium flow processes influence the mass flow rate. A simple way to understand how mass flow rate is affected is to consider how γ changes in the limits of non-equilibrium flow. Eq. (1) shows the dependence of mass flow rate on the specific heat ratio. Specifically, larger values of γ correspond to larger values of C_s and result in increased mass flow rates. The maximum attainable γ and therefore the largest possible mass flow rate occurs in the frozen flow limit when $\gamma^{\text{fr}}=1.4$. Similarly, the minimum possible mass flow rate occurs in the equilibrium flow limit where $\gamma^{\text{eq}}(T)$ attains its minimum value (i.e. $1.29 \leq \gamma^{\text{eq}}(T) \leq 1.345$) for temperatures ranging from 200 to 300 K. Therefore, when vibrational relaxation effects become important, the mass flow increases, achieving some intermediate value between the two limiting mass flow rates.

3.2. Experimental validation of the non-equilibrium model

There has been a significant amount of research done to support applications where vibrational non-equilibrium effects are known to be important, such as flows in hypersonic wind tunnels, chemical lasers, and high temperature gas dynamics. However, the effect of vibrational non-equilibrium on the discharge coefficients of critical nozzles has not been previously investigated. Therefore, as further confirmation of the numerical results, two experiments were designed with the intent of verifying the vibrational relaxation explanation proposed for CO_2 critical nozzle flows. Both experiments set out to ascertain the effects that vibrational relaxation has on C_d by controlling $\Gamma=\tau_{\text{vib}}/\tau_{\text{res}}$ — the primary parameter affecting vibrational relaxation phenomena. The first experiment, conducted at NRLM, varied τ by using various nozzle sizes and by adjusting the stagnation pressure. In this experiment the measured C_{ds} were compared to those predicted by the vibrational non-equilibrium CFD model over a wide range of Reynolds numbers. The second experiment, conducted at NIST,

reduced Γ by adding small concentrations of water vapor to the CO_2 gas.

For a given gas composition the magnitude of Γ determines the extent of the vibrational non-equilibrium effects in the flow field. For values of Γ significantly less than unity (i.e. $\tau_{\text{vib}} \ll \tau_{\text{res}}$) fluid particles equilibrate quickly with the changing thermodynamic surroundings that they encounter while moving along their trajectory. That is, the time that it takes a fluid particle to traverse a certain distance along its trajectory is large relative to the time necessary for molecular collisions to bring the fluid particle into vibrational equilibrium. At larger values of Γ , however, relaxation effects become more important. Physically, fluid particles move along their trajectory passing through their surrounding thermodynamic environment in time periods that are on the same order of magnitude (or shorter) than the time necessary for molecular collisions to bring the level of vibrational energy into equilibrium. Based upon the important role Γ plays in characterizing non-equilibrium flow behavior, both experiments systematically vary this parameter to assess vibrational relaxation effects.

3.2.1. First experiment

The first experiment utilized a gravimetric calibration facility to measure the discharge coefficient of four different size ISO critical nozzles flowing CO_2 gas [28]. The throat diameters of the four nozzles were 0.2950, 0.5935, 1.1845, and 2.3598 mm, respectively. These nozzles were constructed using a super accurate lathing process so that their throat diameters were accurate to within $\pm 1 \mu\text{m}$ [11]. For each nozzle, the stagnation pressure was varied from 50,662.5 Pa to 303,975 Pa while the stagnation temperature remained fixed at 300 K. Although there is some overlap of Reynolds number for the different nozzle sizes, in general, the range of Reynolds number differed for each nozzle due to the different diameter sizes. The Reynolds number ranged from a low of 2.5×10^3 corresponding smallest nozzle size to a high of 1.31×10^5 corresponding to the largest nozzle size.

The eight fold increase in throat diameter sizes as well as the six fold increase in stagnation pressure were used to vary $\Gamma=\tau_{\text{vib}}/\tau_{\text{res}}$. For the ISO nozzles used in this experiment, the larger throat diameters corresponded to longer axial distances between the nozzle inlet and the nozzle throat; therefore, the distance fluid particles had to travel to reach sonic conditions as well as the time necessary to traverse this distance (i.e. flow residence time) increased for larger nozzle sizes. By varying the nozzle sizes the flow residence time can be augmented by a factor of eight, which in turn, leads to an eight fold reduction in Γ . Similarly, the six fold increase in stagnation pressure (at a fixed stagnation temperature of 300 K) reduces the vibrational relaxation time [see Eq. (5)], and consequently Γ by six fold. By varying nozzle

size and stagnation pressure together Γ can be changed by a factor of 48, almost two orders of magnitude.

Given that the Reynolds number is proportional to both P_0 and d , varying these parameters to control $\Gamma = \tau_{\text{vib}}/\tau_{\text{res}}$ result in changes to the Reynolds number as well. In particular, for a fixed gas composition at a constant stagnation temperature ($T_0 = 300$ K), increasing either P_0 or d^6 decreases Γ , but increases the Reynolds number. As a result, relaxation effects diminish at larger Reynolds numbers where Γ is lower. If non-equilibrium effects are responsible for the unusual calibration characteristics observed for CO_2 , a drop off in C_d should be observed in higher Reynolds number calibration data. Specifically, the discharge coefficient should deviate from the linear relationship between C_d and $1/\sqrt{Re_{\text{ideal}}^*}$ observed in laminar flow for gases unaffected by vibrational relaxation effects. Furthermore, since the effect of vibrational relaxation is to increase the mass flow through the nozzle, larger than unity C_d 's are possible at finite Reynolds numbers. This is in spite of the fact that the discharge coefficient is normalized by \dot{m}_{ideal} , the mass flow based on an inviscid analysis.

For gases unaffected by relaxation phenomena (e.g. Air, N_2 , Ar, He, and H_2), C_d increases linearly with decreasing $1/\sqrt{Re_{\text{ideal}}^*}$ over the entire laminar range of Reynolds numbers (i.e. $Re_{\text{ideal}}^* < 10^6$). Experimental documentation of this linear behavior for Air has been demonstrated by Ishibashi and Takamoto [11]. These authors fit calibration data to the expression, $C_d = \alpha + \beta/\sqrt{Re_{\text{ideal}}^*}$ (where α and β are coefficients determined by the fit), and the scatter along the curve was less than $\pm 0.04\%$ over a Reynolds number range from 10^4 to 2.5×10^5 . Additional experimental documentation of this linear trend for other gases (e.g. N_2 , Ar, He, and H_2) can be found in the work of Arnberg et al. [22] This linear behavior is also in agreement with theoretical C_d predictions when either the equilibrium CFD model or the NRLM analytical model is used to predict the discharge coefficient for CO_2 flow.

Fig. 6 compares the experimental data to the three predictive models that were discussed in the previous section. The smallest nozzle size ($d = 0.2950$ mm) corresponds to the lowest Reynolds number range and is denoted by the \square 's. Likewise, the intermediate nozzle sizes $d = 0.5935$ mm and $d = 1.1845$ mm are denoted by the \times 's and \circ 's respectively, and the largest nozzle size ($d = 2.3598$ mm) denoted by the \triangle 's corresponds to the highest values of Reynolds number. The size of the symbols is scaled to the 0.2% experimental uncertainty. The results yielded by the three predictive models are depicted by lines to distinguish them from experimental

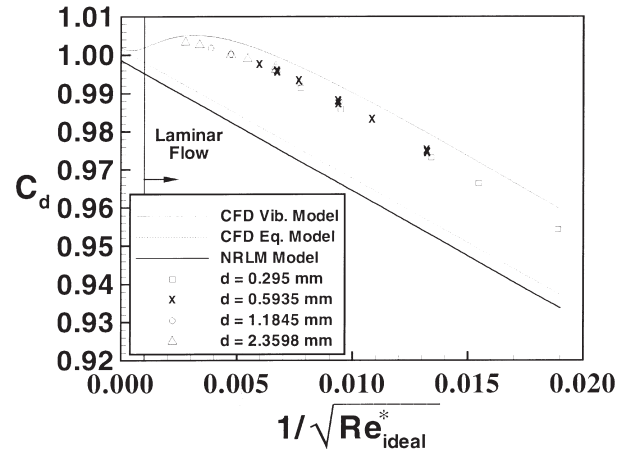


Fig. 6. Comparison of experimental CO_2 calibration data for various toroidal throat nozzle sizes with predictive models.

data. A solid line (—) is used to depict vibrational non-equilibrium CFD results, a dashed line (---) depicts the equilibrium CFD results, and the dotted line (\cdots) is used to depict the NRLM analytical model.

Behavior consistent with vibrational relaxation effects can be observed in the CO_2 calibration data (\square , \times , \circ , and \triangle) in Fig. 6. In particular, at the larger Reynolds numbers (i.e. lower $1/\sqrt{Re_{\text{ideal}}^*}$) Γ decreases so that the magnitude of the slope of the calibration data begins to decrease and the linear characterization of C_d with $1/\sqrt{Re_{\text{ideal}}^*}$ no longer holds. The measured C_d 's are less than would be predicted by extrapolating the linear relationship (between C_d and $1/\sqrt{Re_{\text{ideal}}^*}$) observed at lower Reynolds numbers.

At higher values of Γ , which correspond to lower Reynolds numbers ($2.5 \times 10^3 \leq Re_{\text{ideal}}^* \leq 2.5 \times 10^5$), vibrational relaxation effects are insensitive to changes in Γ — a phenomenon expected of the exponential relaxation processes. As Γ decreases, however, relaxation effects begin to transition toward equilibrium flow behavior, tending to decrease C_d . Given that decreases in Γ correspond to increases in Reynolds numbers, the boundary layer thins, tending to increase C_d . The two competing mechanisms result in a non-linear calibration curve at large Reynolds numbers. In addition to the non-linear calibration behavior, vibrational relaxation effects are also largely responsible for the greater than unity C_d 's observed in the calibration data.

Comparison between the calibration data (\square , \times , \circ , and \triangle) and the vibrational non-equilibrium CFD model (—) in Fig. 6 shows that they are in good agreement. The vibrational non-equilibrium CFD model captures both the linear behavior exhibited at the lower Reynolds numbers as well as the non-linear C_d behavior observed at larger Reynolds numbers. The CFD relaxation model overpredicted the calibration data, but by only 0.4% at the lower Reynolds numbers with better agreement at higher Reynolds numbers. Although the

⁶ ISO nozzles are geometrically scaled so that larger throat diameters correspond to longer distances from the nozzle inlet to the nozzle throat.

experimental facilities were limited to a maximum Reynolds number of 1.31×10^5 , the CFD model was extended beyond this value in order to assess the implications of relaxation phenomenon at still higher Reynolds numbers. For simplicity these computations assume that the boundary layer remains laminar even above the transitional Reynolds number of 10^6 (indicated by the vertical dashed line in Fig. 6. Strictly speaking, above this value the predictions lose their validity, but they are still useful for developing an understanding of relaxation effects isolated from other mechanisms (e.g. real gas effects and transition to turbulence).

Based on the vibrational non-equilibrium CFD predictions in Fig. 6, relaxation phenomenon can be classified into three regimes depending on Γ . For high values of Γ (i.e. lower Reynolds numbers) the discharge coefficient of the nearly frozen flow increases linearly with decreasing $1/\sqrt{Re_{ideal}^*}$ and is approx. 2% larger than would be predicted by equilibrium flow models. As Γ decreases — corresponding to larger Reynolds numbers — the flow begins to transition toward equilibrium flow causing a deviation from the linear relationship between C_d and $1/\sqrt{Re_{ideal}^*}$. As a result of this transition, C_d decreases with increasing Reynolds number. At still lower values of Γ relaxation effects become negligible and C_d predictions return to the equilibrium flow behavior, regaining a linear characterization with $1/\sqrt{Re_{ideal}^*}$.

3.2.2. Second experiment

A second experiment using mixtures of carbon dioxide and water vapor was devised to obtain further evidence that vibrational equilibrium effects are responsible for the observed discharge coefficient phenomenon. It is documented in the literature of vibrational non-equilibrium that small concentrations of water vapor act as a catalyst to CO_2 vibrational relaxation and lead to dramatically smaller values of the vibrational relaxation time, τ_{vib} , and consequently reduced values of Γ [29,30]. By introducing concentrations of 0.5% (or less) water vapor on a molar basis into CO_2 , significant reductions in the discharge coefficient relative to those for pure CO_2 should be observed. For the experiment, a 0.2921 mm throat diameter critical venturi was calibrated with pure CO_2 and with CO_2 diluted by varying concentrations of water vapor. The mass flow was measured with a pressure–volume–temperature–time primary flow standard at NIST with an uncertainty of 0.10% [31]. The CO_2 and water vapor mixture was generated by first adding water vapor to an evacuated tank until the desired partial pressure of water was attained. Then CO_2 was added to the tank until the desired total pressure was attained. The entire experimental apparatus was kept in a room heated to 300 K to prevent condensation of water vapor during the course of the experiment. (The dew point temperature of the 0.5% water vapor mixture is 286.4 K at the

largest operating stagnation pressure of 303,975 Pa). In addition, before and after usage of the gas mixture, an optical hygrometer was used to measure the dew point temperature of the mixture and a total pressure measurement was made at the hygrometer. Using these measurement techniques, the uncertainty of the water vapor concentration is 0.05% or less.

The results of the CO_2 and water vapor mixture experiment are shown in Fig. 7. It can be seen that the addition of 0.5% water vapor to the CO_2 gas reduced the discharge coefficient by about 1.3%, moving the discharge curve in the direction anticipated by the vibrational relaxation explanation. The addition of water vapor reduces the vibrational relaxation time of the gas mixture which in turn reduces the mass flux through the venturi throat as explained previously.

In calculating the discharge coefficients in Fig. 7, the normalizing theoretical mass flow includes a version of C_s based on the methods described by Aschenbrenner [32] (i.e. weighting the pure gas specific heats by their respective mole fractions to obtain the mixture specific heat ratio). Also the gas constant for the mixture was calculated by weighting the pure gas component molecular weights by the respective mole fractions. In this way, the known major effects on the discharge coefficient have been taken into account in the normalizing quantity of the discharge coefficient and remaining changes in the discharge coefficient can be attributed largely to vibrational relaxation effects.

4. Conclusions

Computational Fluid Dynamics was utilized to make C_d predictions for CO_2 gas flow through various sizes of ISO [4] critical nozzles (i.e. 0.2950, 0.5395, 1.1845, and 2.3598 mm) over a Re_{ideal}^* range from 2500 to

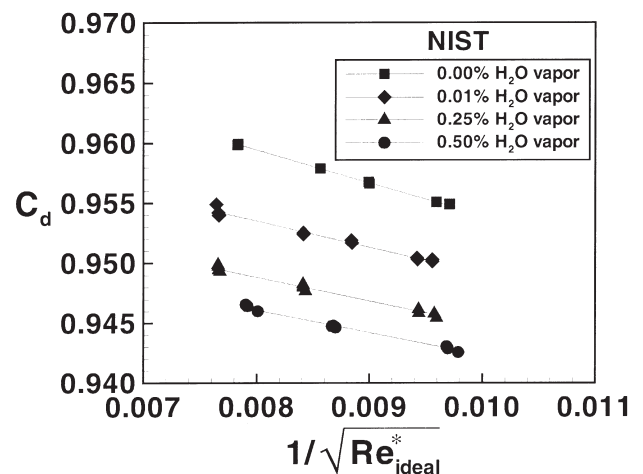


Fig. 7. NIST experimental data showing the effect of small concentrations of water vapor on the discharge coefficient of CO_2 .

131,000. When the CFD algorithm included vibrational non-equilibrium effects the error in C_d predictions was reduced by a factor of five over previous models. Moreover, the CFD results were in good agreement with the experimental calibration data, differing by no more than 0.4% at lower Reynolds numbers, and improving at larger Reynolds numbers.

The proposition that vibrational relaxation effects can significantly influence C_d behavior for CO_2 critical nozzle flows was confirmed by two independent experiments as well as the numerical results. The non-equilibrium CFD model showed that vibrational relaxation phenomenon increases the mass flow through the nozzle, and consequently the discharge coefficient. Both experiments demonstrated the significance of Γ , the ratio of vibrational relaxation time to flow residence time in characterizing vibrational non-equilibrium behavior. The first experiment verified an anticipated drop off in C_d at low values of Γ . This behavior was in agreement with the vibrational non-equilibrium explanation and it was also predicted by the vibrational non-equilibrium CFD model. The second experiment, which reduced vibrational relaxation effects by diluting CO_2 with small concentrations of water vapor, also confirmed an expected decrease in C_d .

Vibrational relaxation effects are only significant for certain gas species. In this paper CO_2 gas flow was used to demonstrate the dramatic effect that vibrational non-equilibrium flow processes can have on C_d behavior. The effect of this phenomenon is to increase the mass flow through the nozzle, and consequently the discharge coefficient. In fact, this phenomenon is largely responsible for the nearly 3% offset between the calibration curve of CO_2 and other gases (e.g., N_2 , He, and air). Additionally, vibrational relaxation is mostly responsible for the greater than unity C_d values observed for CO_2 over certain Reynolds number ranges. In future work, it is anticipated that this mechanism can explain species dependent behavior noted for other gases, enhancing our understanding of critical nozzle flows and enabling improved predictive capabilities.

Present analytic models, valid for constant γ , characterize C_d as a function of γ and Re_{ideal}^* . Additional parameters must be considered to account for non-equilibrium flow effects. Based on the experimental results and the vibrational non-equilibrium CFD model, we reason that these additional parameters are $\Gamma = \tau_{vib}/\tau_{res}$, the ratio of vibrational relaxation time to residence time, and ϵ_{vib}/ϵ , the ratio of vibrational energy to overall internal energy. The first parameter, Γ , determines if vibrational non-equilibrium effects are present in the flow field. The limiting values of this parameter range from zero (i.e. equilibrium flow) to infinity (i.e. frozen flow), where intermediate values give an indication of how far the flow is from equilibrium. The second parameter, ϵ_{vib}/ϵ , measures the importance of non-equilibrium effects (if

they are present) in the flow field.⁷ When these additional parameters are considered, non-equilibrium effects can be characterized for all gas species over all flow conditions.

Due to the mathematical complexity of non-equilibrium flows, a rigorous analytical treatment including all of the non-equilibrium flow physics is prohibitively difficult. Nevertheless, close form analytic solutions may still be attainable by making the appropriate simplifying assumptions. Although these assumptions will result in reduced accuracy, they will yield algebraic expressions for C_d behavior, avoiding the more costly and time consuming numerical methods. One possible approximate method involves defining an effective specific heat ratio, γ_{eff} , to use in place of γ in the existing two parameter model. The physical justification of this assumption follows from an examination of γ at the limits of non-equilibrium flow. For equilibrium flow, the specific heat ratio attains its minimum value [i.e. $\gamma = \gamma^{eq}(T)$]. Similarly, the specific heat ratio attains its maximum value (i.e. $\gamma = \gamma^{fr}$) for frozen flow, and γ_{eff} must be defined between these limiting values. While the value of γ_{eff} should in some way depend on Γ and ϵ_{vib}/ϵ , developing a method for its prediction is a topic of future research. It should be pointed out, however, that even if a suitable method for choosing γ_{eff} is found, this phenomenological model does not capture all the physics of non-equilibrium flow.

All analysis in this paper were done for a limited range of temperatures, pressures, and nozzle sizes. Vibrational non-equilibrium would be more important at elevated temperatures given that the contribution of the vibrational energy to the overall internal energy increases. For gases that have non-negligible vibrational energy levels, relaxation phenomenon will be an issue for values of Γ close to (or greater than) unity. Physically, this condition is most likely to occur for small throat diameter ISO nozzles when they are calibrated at low stagnation pressures.

Acknowledgements

Computational support was provided by the High Performance Systems and Service Division of the Information Technology Laboratory at NIST. In addition, enlightening discussions with Drs Pedro Espina, George Mattingly, Peter Rothfleisch, and Greg Rosasco of NIST are gratefully acknowledged.

References

- [1] J.D. Wright, The long term calibration stability of critical flow nozzles and laminar flowmeters, in: NCSL Conference Proceedings Albuquerque, NM, 1998, pp. 443–462.

⁷ Here it is important that the energy datum is taken to be the energy of the molecule at absolute zero (i.e. the zero-point energy)

- [2] M. Takamoto, M. Ishibashi, N. Wantanabe, A. Aschenbrenner, S. Caldwell, Intercomparison tests of gas flow rate standards, in: Proceedings of the 6th International Conference on Flow Measurement Seoul, Korea, 1993, pp. 75–82.
- [3] J.D. Wright, G.E. Mattingly, S. Nakao, Y. Yokoi, M. Takamoto, Intercomparison tests of NIST primary standard with NRLM transfer standard for small mass flow rates of nitrogen gas, *Metrologia* 35 (1998) 211–221.
- [4] ISO 9300: 1990 (E), Measurement of gas flow by means of critical flow venturi nozzles, Geneva, Switzerland, 1990.
- [5] J.E.A. John, Gas Dynamics, Allyn & Bacon, Newton, MA, 1984.
- [6] B.S. Stratford, The calculation of the discharge coefficient of profiled choked nozzles and the optimum profile for absolute air flow measurement, *J. Royal Aeron. Soc.* 68 (1962) 237–245.
- [7] B. Masure, J.L. Solignac, P. Laval, Mass flow rate measurement by means of a sonic throat, Office National d'Etudes et de Recherches Aérospatiales (ONERA), 1971.
- [8] I.M. Hall, Transonic flow in two-dimensional and axially-symmetric nozzles, *Q. J. Mech. Appl. Math.* 15 (4) (1962) 487–508.
- [9] D. Geropp, Laminare Grenzschichten In Ebenen Und Rotationssymmetrischen Lavalduesen, Deutsche Luft Und Raumfahrt, Forschungsbericht, 1971, pp. 71–90.
- [10] S.P. Tang, Theoretical dependence of the discharge coefficients of axisymmetric nozzles under critical flows, Technical Report PR-118-PU, Department of Mechanical Engineering, Princeton University, 1969.
- [11] M. Ishibashi, M. Takamoto, Very accurate analytical calculation of the discharge coefficients of critical venturi nozzles with laminar boundary layer, in: Proceedings of the FLUCOME Hayama, Japan, 1997.
- [12] G.E. Mattingly, Gas flowrate metrology, NCSL Conference Proceedings, Vol. 29, 1988, pp. 9–16.
- [13] J.D. Wright, G.E. Mattingly, NIST calibration services for gas flow meters: piston prover and bell prover gas flow facilities, NIST SP 250-49, 1998.
- [14] H.W. Coleman, W.G. Steele, Experimentation and Uncertainty Analysis for Engineers, Wiley, New York, 1989.
- [15] S. Tang, Discharge coefficients for critical flow nozzles and their dependence on reynolds numbers, Ph.D. dissertation, Department of Mechanical Engineering, Princeton University, Princeton, NJ, 1969.
- [16] S. Nakao, T. Hirayama, M. Takamoto, Effects of thermalphysical properties of gases on the discharge coefficients of the sonic venturi nozzle, in: Proceedings of the 1997 ASME Fluids Engineering Division Summer Meeting Vancouver, BC, Canada, 1997.
- [17] A.N. Johnson, C.L. Merkle, P.I. Espina, G.E. Mattingly, J.D. Wright, Numerical characterization of the discharge coefficient in critical nozzles, in: NCSL Conference Proceedings Albuquerque, NM, 1998, pp. 407–422.
- [18] C.H. Kruger, W.G. Vincenti, Introduction to Physical Gas Dynamics, Wiley, New York, 1965.
- [19] L. Landau, E. Teller, Zur Theorie der Schalldispersion, *Physik Z. Sowjetunion* 10 (1) (1936) 34.
- [20] A.F. Estrada-Alexanders, J.P.M. Trusler, Speed of sound in (0.4C₂H₆+0.6CO₂) at temperatures between $T=220$ K and $T=450$ K and pressures up to $P=1.2$ MPa, *Journal of Chemical Thermodynamics* 31(5) (1999).
- [21] J. Hilsenrath, C.W. Beckett, W.S. Benedict, L. Fano, H.J. Hoge, J.F. Masi, R.L. Nuttall, Y.S. Touloukian, H.W. Wooley, Tables of thermal properties of gases, US Department of Commerce NBS Circular 564, 1955.
- [22] B.T. Arnborg, C.L. Britton, W.F. Seidl, Discharge coefficient correlations for circular-arc venturi flowmeters at critical (sonic) flow, *ASME Journal of Fluids Engineering* June (1974).
- [23] P. Buelow, S. Venkateswaran, C.L. Merkle, The effect of grid aspect ratio on convergence, *AIAA Journal* 32 (1994) 2401–2406.
- [24] J. Feng, C.L. Merkle, Evaluation of preconditioning methods for time marching systems, AIAA Paper 90-0016, AIAA 28th Aerospace Sciences Meeting, Reno, NV, 1990.
- [25] P.E.O. Buelow, Convergence enhancement of Euler And Navier–Stokes algorithms, Ph.D. dissertation, Department of Mechanical Engineering, Pennsylvania State University, University Park, PA, 1995.
- [26] C.H. Edwards, D.E. Penny, Elementary Differential Equations With Boundary Value Problems, Prentice–Hall, Englewood Cliffs, NJ, 1989.
- [27] P. DuChateau, D. Zachmann, Applied Partial Differential Equations, Harper & Row, New York, 1989.
- [28] S. Nakao, Y. Yokoi, M. Takamoto, Development of a calibration facility for small mass flow rates of gas and the uncertainty of a sonic venturi transfer standard, *Flow Meas. Instrum.* 7 (1996) 77–83.
- [29] K.F. Herzfeld, T.A. Litovitz, Absorption and Dispersion of Ultrasonic Waves, Academic Press, New York, 1959.
- [30] L.E. Kinsler, F.R. Austin, A.B. Coppens, J.V. Sanders, Fundamentals of Acoustics (3rd ed), Wiley, New York, 1982.
- [31] L. Olsen, G. Baumgarten, Gas flow measurement by collection time and density in a constant volume, flow: its measurement and control in science and industry. ISA (1971) 1287–1295.
- [32] A. Aschenbrenner, The influence of humidity on the flowrate of air through critical flow nozzles. *FLOMEKO* (1983) 61–64.